RSC Advances

PAPER

View Article Online
View Journal | View Issue

Open Access Article. Published on 13 January 2017. Downloaded on 10/20/2025 1:41:01 AM.
This article is licensed under a Creative Commons Attribution 3.0 Unported Licence.

Cite this: *RSC Adv.*, 2017, 7, 3635

Catalytic impact of alloyed Al on the corrosion behavior of $Co_{50}Ni_{23}Ga_{26}Al_{1.0}$ magnetic shape memory alloy and catalysis applications for efficient electrochemical H_2 generation†

Mohammed. A. Amin,*[ab] Nader El-Bagoury,[ac] M. H. H. Mahmoud,[ac] M. M. Hessien,[ac] Sayed S. Abd El-Rehim,[b] Joanna Wysocka[d] and Jacek Ryl[d]

The electrochemical and corrosion behaviour of $Co_{50}Ni_{23}Ga_{27-x}Al_x$ (x = 0 and 1.0 wt%) magnetic shape memory alloys (MSMAs) was studied in 0.5 M NaCl solutions using various electrochemical techniques. Results showed remarkable activation of the tested MSMA toward pitting corrosion upon alloying it with Al. XPS examination confirmed the activation influence of alloyed Al. It proved that the presence of Al in the alloy's matrix weakens its passivity, as manifested by a lower amount of gallium oxides and Cl^- adsorption in the aluminium containing MSMA sample. Alloyed Al also activated significantly the tested MSMA for the hydrogen evolution reaction (HER), as indicated by cathodic polarization, electrochemical impedance spectroscopy (EIS), and faradaic efficiency (FE) measurements. Such measurements were performed in 0.1 M KOH solutions and showed that the $Co_{50}Ni_{23}Ga_{26}Al_{1.0}$ alloy is much more active for the HER than Co, Ni, $Co_{50}Ni_{50}$, and $Co_{50}Ni_{23}Ga_{27}$ electrodes. The catalytic impact of pitting corrosion, proved to be catalyzed by Al, on the HER activity of the CoNiGaAl alloy was also studied. The pitted $Co_{50}Ni_{23}Ga_{26}Al_{1.0}$ MSMA, the best catalyst here, exhibited high HER catalytic performance with an exchange current density (j_o) of 0.2 mA cm^{-2} and FE 96%, and thus approached Pt/C (j_o = 0.6 mA cm^{-2} and FE ~ 100%). Our best catalyst also showed good stability and durability after 3000 cycles of cathodic polarization between the corrosion potential (E_{corr}) and −1.0 V *vs.* RHE, and 24 h of electrolysis at a high cathodic current density of 100 mA cm^{-2}. Microstructure changes made by Al, together with findings obtained from SEM/EDX mapping and XPS studies, were used to interpret its activation influence towards the HER.

Received 17th October 2016
Accepted 24th November 2016

DOI: 10.1039/c6ra25384a

www.rsc.org/advances

1. Introduction

Shape memory alloys (SMAs) are an important class of smart materials that have the ability to remember a shape. These alloys are unique materials having a different philosophy than the commercial ones, such as steel and titanium alloys. Large recoverable shape change is observed as a result of cooperative motion of atoms, which is the result of diffusion-less solid–solid phase transformation. The time-independent solid–solid phase transformation can be triggered by change in temperature, stress or magnetic field.[1–3] Current practical uses of SMAs are limited to below 100 °C which is the limit for the transformation temperatures of most commercially successful SMAs such as NiTi and Cu-based alloys.

A new class of these materials, termed as magnetic shape memory alloys (MSMAs), has recently discovered. Such materials have received much attention as they undergo both magnetic field induced strain and magnetic shape memory effect. This interesting effect has been first discovered in the Ni–Mn–Ga system.[4,5] So far, the highest field-induced strain was only achieved for off-stoichiometric single crystals,[6,7] where application of an external magnetic field has resulted in a strain of up to 10%.[7] These changes provided this class of materials with additional properties, such as the elastocaloric and magnetocaloric effects.[8,9] Such properties are of interest for applications in solid state cooling near to the room temperature.[10] But, bulk polycrystalline materials are of technological interest, as they are easier to produce and less expensive than the single crystal ones. In addition, the fragility of single crystal MSMAs limits their practical applications. For these reasons, numerous

[a]Materials Science and Engineering Group, Department of Chemistry, Faculty of Science, Taif University, 888 Hawiya, Saudi Arabia. E-mail: maaismail@yahoo.com
[b]Department of Chemistry, Faculty of Science, Ain Shams University, 11566 Abbassia, Cairo, Egypt
[c]Central Metallurgical Research and Development Institute (CMRDI), P.O. Box: 87 Helwan, Cairo, Egypt
[d]Department of Electrochemistry, Corrosion and Materials Engineering, Chemical Faculty, Gdańsk University of Technology, Narutowicza 11/12, 80-233 Gdańsk, Poland

† Electronic supplementary information (ESI) available. See DOI: 10.1039/c6ra25384a

Open Access Article. Published on 13 January 2017. Downloaded on 10/20/2025 1:41:01 AM.
This article is licensed under a Creative Commons Attribution 3.0 Unported Licence.

studies have been performed on several candidates for MSMAs to find out new alternative materials with lower price and brittleness. These alternatives include: Fe–Pd,[11] Fe–Pt,[12] Ni–Mn–Al,[13] and Co–Ni–Al.[14,15] Recently, Ni–Fe–Al[16] and Co–Ni–Ga[17] have been emerged as new MSMAs, which are good alternatives to NiMnGa alloys, as they contain a γ phase capable of improving their ductility.

Since under application conditions MSMAs may undergo some corrosion problems,[18] corrosion research studies on MSMAs have become essential. However, literature revealed very limited number of publications concerning corrosion behaviour of these materials.[18–20] In addition, and to the best of our knowledge, there are no reports in the literature concerning the effect of Al addition as an alloying element on the corrosion behaviour of CoNiGa MSMA.

Successful electrode materials for the HER have to be stable, showing no signs of corrosion or passivation while having low overpotential. Paunovic *et al.*[21] investigated numerous modifications of CoNi SMA concluding the necessity of further modification to increase the catalytic activity of HER.

Morphology, microstructure, internal stress and catalytic ability of the layers are strongly influenced by the structure of the substrate. In particular, morphology of alloy has a decisive influence on the kinetics of the surface redox reaction. The most practical approach to overcome the kinetic and diffusional limitations is to increase the real surface area of the electrode. Several studies on CoNi alloys report performance of submicron size powder electrodes,[22] porous foams,[23] or even encapsulating CoNi nanoalloys in ultrathin layers of graphene.[24] Unlike other attempts to replace precious-metal-based electrocatalysts of HER, lowering efficiency and stability of such compounds, CoNi@C fabricated by Deng *et al.*[24] are claimed to possess high performance. The optimized catalyst exhibits high stability and activity with an onset overpotential of almost zero *versus* the reversible hydrogen electrode (RHE) and an overpotential of only 142 mV at 10 mA cm^{-2}, which is quite close to that of commercial 40% Pt/C catalysts.

On the other hand, electrochemical properties of thermally treated CoNiGa MSMA were investigated by Sanchez-Carrillo *et al.*[25] It was revealed, that thermal treatments improve corrosion properties of alloy in neutral and acidic solutions while chlorides prevent spontaneous passivation which is otherwise observable at anodic oxidation.

Based on the literature presented above, the objective of the present work is two-fold; first, to study the effect of Al addition on the anodic behavior (including passivity and its breakdown and subsequent formation of pits and their repassivation) of the CoNiGa MSMA. It was also the purpose of this part to use chronoamperometry measurements to study the role of Al in the growth kinetics of the passive layer and pits. Such corrosion studies were performed in 0.5 M NaCl solutions. SEM/EDX and XPS examinations were used to study morphologies and compositions of the corroded surfaces devoid of and containing the alloyed Al.

The second objective of the present work is to evaluate, for the first time, the impact of alloyed Al on the electrocatalytic activity of CoNiGaAl SMA for the HER. HER activity measurements were conducted in deaerated aqueous KOH solutions (0.1 M) using linear sweep voltammetry and electrochemical impedance spectroscopy techniques. The HER activity of the best catalyst (the pitted CoNiGaAl MSMA) approached that of Pt/C. Such corrosion pretreatment, together with the activation influence of alloyed Al, led to the formation of deep pits with edges and walls proved to be active for the HER. Thus, pitting corrosion (a highly undesirable process) can be used to fabricate catalysts for wide applications. This may turn the attention of a number of researchers for future studies covering the title "pitting corrosion for useful materials fabrication".

2. Experimental

2.1. Materials and solutions

Both of $Co_{50}Ni_{23}Ga_{27}Al_0$ and $Co_{50}Ni_{23}Ga_{26}Al_1$ alloys were produced by using arc-melting for the pure elements (99.99 wt% Co, 99.99 wt% Ni, 99.99 wt% Ga and 99.99 wt% Al) under controlled atmosphere (argon gas), in a water-cooled copper crucible. To get high level of homogenization, these alloys were melted for four times. After casting, both alloys were sliced into small-sized parts to be used in the various experimental studies. The same procedure was used for the manufacture of the $Co_{50}Ni_{50}$ alloy, which was used in HER catalytic activity measurements for comparison. These alloys were cast as cylindrical rods for the electrochemical tests. These rods machined carefully and mounted in polyester resin after the electric contact, with special care taken to prevent the presence of crevices. The exposed area was ~1.0 cm^2. Before each run, the samples were wet ground with 600-grit silicon carbide (SiC) paper and finally washed in distilled water, followed by immediate rinsing with absolute ethanol. The microstructural changes were investigated by a scanning electron microscope (JEOL JSM5410). The equilibrium phase composition was detected by an energy X-ray dispersive spectroscopy (EDS) attached to SEM. For the metallography study, agent of Nital's (15% nitric acid in ethanol) was used as chemical etching.

All solutions used in this study were analytical grade chemical reagents purchased from Sigma-Aldrich. These solutions were freshly prepared using water purified by a Millipore Milli-Q system (resistivity: 18.2 MΩ cm).

2.2. Electrochemical study

A standard jacketed three-electrode cell was used for electrochemical measurements. A Pt electrode and a saturated calomel electrode (SCE) were used as auxiliary electrode and reference electrode, respectively. All potentials were measured against SCE. Electrochemical experiments were performed *via* connecting the cell to a potentiostat/galvanostat AUTOLAB (PGSTAT30) coupled to an Autolab frequency response analyzer (FRA) with FRA2 module connected to PC. Measurements were conducted in a 200 ml test solution (large enough to resist significant drifts in composition during the run). Prior to any electrochemical run, oxygen was removed from the test solutions by bubbling Ar through the solution for at least 30 min. The temperature was set at (25 °C ± 0.2 °C) using a temperature-

Open Access Article. Published on 13 January 2017. Downloaded on 10/20/2025 1:41:01 AM. This article is licensed under a Creative Commons Attribution 3.0 Unported Licence.

controlled bath with water circulating through the outer cell jacket.

For each electrochemical run, at least three separate experiments were performed to ensure results' reproducibility. Data obtained were found to be statistically significant. We calculated and reported their arithmetic mean and standard deviation accordingly.

2.2.1. Uniform corrosion studies. Tafel extrapolation, LPR, and EIS methods were used to study the uniform corrosion behavior of the studied alloys. The working electrode is first stabilized in the test solution for 2 h, then EIS, LPR and Tafel polarization measurements were consecutively conducted. The former was carried out at E_{corr} using AC signals of amplitude 5 mV peak-to-peak in the frequency range 100 kHz to 1.0 mHz. For LPR measurements, the potential of the working electrode is swept from −20 to +20 mV *versus* E_{corr} at an extremely slow scan rate of 0.167 mV s^{-1} starting from more negative potential to the anodic direction. Finally, Tafel polarization measurements were conducted *via* sweeping the potential of the working electrode within the Tafel potential region ($E = E_{corr} \pm 250$ mV) using a scan rate of 1.0 mV s^{-1}.

ICP-AES (inductively coupled plasma atomic emission spectrometry) was also employed as an independent method of chemical analysis to confirm results obtained from polarizations and impedance measurements. In this method, the concentrations of both Ni^{2+} and Co^{2+} ions were determined for each alloy in 0.5 M NaCl solutions at 25 °C as a function of the time of immersion. In this respect, full immersion tests (1–15 days) were performed following the ASTM-G31 standard.[26] The obtained results are collected in Table S2 (ESI†), where the amounts of Ni^{2+} and Co^{2+} ions released from the alloy into the corrosive medium, as a result of the aggressive attack of Cl^-, were taken as a measure of the corrosion rate. ICP measurements were performed using Perkin-Elmer Optima 2100 Dual View inductively coupled plasma atomic emission spectrometry (ICP-AES) instrument connected with AS 93 Plus autosampler.

2.2.2. Anodic behaviour (passivity and pitting corrosion). The effect of Al addition on passivity, breakdown of passivity, pitting corrosion, and repassivation processes of CoNiGa SMA have been studied in 0.5 M NaCl solutions using cyclic polarization and chronoamperometry measurements. For cyclic polarization measurements, the working electrode is first stabilized for 2 h at the rest potential, then scanned linearly from a starting cathodic potential of −2.0 V(SCE) with scan rate 5.0 mV s^{-1} till an ending anodic potential of 1.0 V(SCE), then reversed direction with the same scan rate till the starting potential to form one complete cycle. Chronoamperometric (current *vs.* time) measurements were recorded at a fixed anodic potential (E_a) after a two step procedure. The working electrode, after being held at a starting cathodic potential of −2.0 V(SCE) for 60 s to attain a reproducible electro-reduced electrode surface, was anodically polarized at a scan rate of 5.0 mV s^{-1} till E_a is reached. Then, finally held at the required E_a for 5.0 min where the passing anodic current was recorded against time.

2.2.3. HER activity. Linear potential sweep voltammetry (LSV) and electrochemical impedance spectroscopy (EIS) techniques were used to evaluate the HER electrocatalytic activity of the tested alloys. The HER catalytic performance of pure Co (99.99 wt%), pure Ni (99.99 wt%), and $Co_{50}Ni_{50}$ alloy electrodes were studied for comparison. A commercial 20 wt% Pt/C catalyst (used as received) was also employed as the standard. A homogeneous, well-dispersed ink of the Pt/C catalyst was prepared by dispersing 4 mg of it in 2 ml of 9 : 1 v/v water/Nafion by sonication. Typically, 5 μl of this catalyst ink were covered on a glassy carbon electrode (3 mm in diameter) and then dried in an ambient environment for measurements. The Pt/C catalyst was prepared with a catalyst loading of ∼0.14 mg cm^{-2}. Measurements were conducted in deaerated 0.1 M KOH solutions. To run a LSV experiment, the working electrode is cathodically scanned starting from the corrosion potential (E_{corr}) at a scan rate of 5.0 mV s^{-1} up to a cathodic potential of −1.0 V *vs.* SCE. All potentials in the HER study were converted from the SCE scale to that of the reversible hydrogen electrode (RHE), as described in the ESI file,† Section 1. Impedance measurements were performed at selected cathodic overpotential values, employing AC signals of amplitude 5 mV peak to peak covering the frequency range 100 kHz to 10 mHz.

The durability and stability of the best catalyst was evaluated by 24 h of galvanostatic measurements at a fixed cathodic current density of 100 mA cm^{-2} and continuous cathodic potential cycling. For potential cycling, the potential was swept linearly from the starting potential (E_{corr}) towards the cathodic direction at a scan rate of 50 mV s^{-1} till a catholic potential of −1.0 V *vs.* RHE, and then reversed with the same scan rate till the starting potential to form one complete cycle. The process of cycling was repeated 3000 times without withdrawing the electrode from the solution and without time delay. Measurements were carried out in deaerated 0.1 M KOH solutions at 25 °C.

2.2.3.1. Faradaic efficiency for the HER. Faradaic efficiencies of the studied catalysts towards the HER were evaluated *via* quantifying the amount of H_2 liberated during a controlled potential electrolysis by a gas chromatography. Then, this measured amount of H_2 is divided by the amount of H_2 calculated from the charge passed (assuming 100% faradaic efficiency) through the working electrode (WE) during that electrolysis. See more details in the ESI file,† Section 2.

2.3. Characterization techniques

Morphology, elemental composition, and mapping studies of the pitted surfaces were performed using an Analytical Scanning Electron Microscope JEOL JSM 6390 LA with an EDS attachment (JEOL EDS EX-54175JMU) on the JEOL SEM. X-Ray photoelectron spectroscopy (XPS) investigation was carried out using Escalab 250Xi (ThermoFisher Scientific, United Kingdom) to determine chemical binding properties of the surface, utilizing monochromatic Al Kα source gun and a spot diameter of 650 μm with charge neutralization implemented by means of a flood gun. High-resolution spectra used during deconvolution were recorded at a pass energy 10 eV and energy step size of 0.1 eV. In order to normalize spectroscopic measurements, binding energy (BE) was calibrated for peak characteristics of neutral carbon 1s (BE = 284.6 eV). Data

Open Access Article. Published on 13 January 2017. Downloaded on 10/20/2025 1:41:01 AM.
This article is licensed under a Creative Commons Attribution 3.0 Unported Licence.

analysis was performed using Avantage v.5 software provided by the manufacturer.

3. Results and discussion

3.1. Cyclic polarization measurements (passivity, pitting corrosion, and repassivation processes)

Fig. 1 shows cyclic polarization curves (linear and logarithmic scales) measured for CoNiGa (alloy I) and CoNiGaAl (alloy II) SMAs in 0.5 M NaCl solution at 25 °C. The two cyclic voltammograms were recorded between −2.0 V(SCE) and +1.0 V(SCE) at a scan rate of 5.0 mV s^{-1}.

It follows from Fig. 1(a_1) that for the two tested alloys on positive going scan, the cathodic current density decreases gradually reaching a zero value at the corrosion potential (E_{corr}). The uniform corrosion accelerating influence of alloyed Al is obvious from the cathodic and anodic polarization curves around E_{corr} (E_{corr} ± 300 mV), Fig. 1(a_2), and deserves further investigations. In this respect, the effect of alloyed Al on the uniform corrosion behavior of the two tested MSMAs is systemically studied employing various electrochemical techniques, and complemented with ICP-AES method of chemical analysis and SEM examinations (ESI, Fig. S1–S4 and Tables S1 and S2†). The objective is to gain insights into the uniform corrosion activation influence of alloyed Al. This will help interpret for the first time, as will be shown later, the catalytic impact of the free corrosion process, which is catalyzed by Al and led to the formation of pits on the surface of alloy II (ESI, Fig. S4†), for the HER.

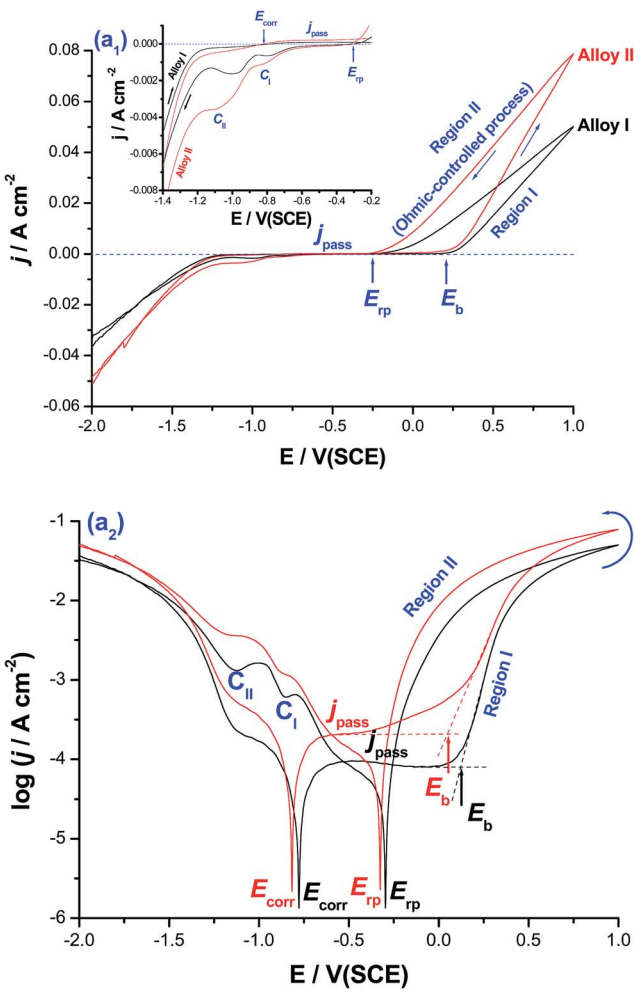

Fig. 1 Cyclic polarization curves (upper) linear and (lower) logarithmic scales recorded for CoNiGa (alloy I) and CiNiGaAl (alloy II) in 0.5 M NaCl solution at 25 °C. Measurements were conducted between −2.0 V(SCE) and +1.0 V(SCE) at a scan rate of 5.0 mV s^{-1}.

Referring again to Fig. 1, it is obvious that the polarization curves lack active dissolution near E_{corr} due to passivation (as evidenced from XPS measurements, see later). Passivity of such alloys extends with a very low passive current (j_{pass}) up to a certain critical potential (designated here as the breakdown potential, E_b), where passivity breakdown and initiation of pitting attack occur. Breakdown of passivity and subsequent formation of pits initiate as a result of the adsorption of Cl^- anions on the oxide/solution interface assisted by applied electric field.[27] This adsorption process is favored at the active sites (defects and flawed regions[27]) of the passive layer and occurs in competition with the passivating (passive layer forming) species, namely dissolved O_2, H_2O molecules and OH^-.[28–30] Following adsorption, a chemical reaction occurs between the adsorbed Cl^- anions and metal cations within the passive oxide film,[31] forming M–Cl soluble species.[29–32] Once formed, the soluble species leave the oxide lattice and goes in solution, causing thinning and localized dissolution of the oxide film.[31] Once the passive film is locally dissolved, pit nucleates at E_b and dissolution of the base metal commences. When the potential exceeds E_b, pit initiates. This in turn makes the medium locally acidic (where the solution chemistry inside the pit is different from that outside it[28,29]), hence allowing for efficient oxide dissolution and pit growth.[28–31] This makes j_{pass} increase drastically (region I).

Upon reversing the potential, the high-current regime (where the backward scan passes over the forward one) is maintained down to a potential known as the repassivation potential (E_{rp}), region II, and a current hysteresis loop (characteristic of the pitting corrosion phenomena[32]) results. This loop indicates a delay in repassivation of an existing pit, the one that is formed during the forward scan (region I), when the potential is swept back negative. The location of E_{rp}, defined as the potential on the reverse scan at which the anodic current becomes zero (*i.e.*, the current changes polarity),[32–34] with respect to E_{corr} is well-defined in the log j *vs.* E plot, Fig. 1(a_2). In pitting corrosion studies, E_{rp} is the relevant potential instead of E_b, as the former helps establish the passive and pitting potential regions of the system. Further inspection of Fig. 1(a_2) reveals that E_{rp} is cathodic with respect to the potential necessary to activate the surface (*i.e.*, towards passivity breakdown and initiation of pitting attack) on the forward potential scan, namely E_b. That means the anode is quite immune at potentials (E) more negative than E_{rp}, where the electrode is protected by an oxide film and pitting will only take place at more positive potentials,[32–34] and also safe from pitting attack within the region $E_{rp} < E < E_b$. This safe location of E_{rp} denotes that the electrode is able to repassivate after the breakdown of the passive film has

Open Access Article. Published on 13 January 2017. Downloaded on 10/20/2025 1:41:01 AM.
This article is licensed under a Creative Commons Attribution 3.0 Unported Licence.

occurred. On the contrary, other systems such as such as Zn/NO_3^- (ref. 33) and Al/gluconate,[34] found it difficult to repassivate since their E_{rp} values locate outside the passive region, thus suffering from severe pitting in these media during the reverse scan.

It is worth referring here to the linear *j–E* relationship observed in region II, Fig. 1(a_1), which suggests an ohmic-controlled process. This process can be explained on the basis of pit growth and subsequent salt film formation.[35–37] During pit growth, the concentration of metallic cations increases gradually due to the active dissolution within the pit. This active dissolution of the base metal continues till the saturated concentration is reached, and a salt film is subsequently formed at the bottom of the pit. The electric field applied across the salt film drives the dissolved metallic cations to move outward through the film. The stronger the field is, the faster the metallic cations move through the film. Hence, in this stage the growth of the pit is controlled by the ohmic potential drop across the salt film.[35–37] At more cathodic potentials, two distinct cathodic current peaks (C_I and C_{II}) are formed. These two peaks are most probably assigned to the reduction of the free metal cations formed through the pits and the salt film (corrosion products) formed during pit growth.

Charge passage measurements showed that the total charge passed between E_b and E_{rp} (regions I and II) for alloy II, that is alloyed with Al, was 38.9 C cm^{-2}, which is ~2.0 times greater than that recorded for alloy I (19.92 C cm^{-2}), the Al-free alloy. The same trend was observed for the two cathodic peaks. In addition, j_{pass} values at any given anodic potential (E_a) within the passive region are always greater, particularly when E_a is approaching E_b, for alloy II than those measured for alloy I. This increase in j_{pass} of alloy II with E_a is quite clear in Fig. 1(a_2). The increase in j_{pass} with E_a refers to general weakness and thinning of the passive film as a result of Cl^- adsorption, which promotes as E_a is made more positive.[28] It seems therefore that the presence of alloyed Al in the matrix of alloy II weakens its passivity promoting Cl^- adsorption, as supported by XPS (see later). On the other hand, the low values of j_{pass} recorded for alloy I reflect the increased resistance of that alloy towards pitting corrosion. Also, E_b of alloy II is achieved at potentials more negative (active) than that of alloy I, as clearly seen in Fig. 1(a_2). These findings are sufficient to conclude that alloy II is more susceptible to pitting corrosion in these solutions than alloy I.

3.2. Chronoamperometry measurements

Chronoamperometry (current *vs.* time) measurements were also performed to confirm the above findings and gain more information about the influence of alloyed Al on the kinetics of the passive layer growth and its breakdown. Fig. 2(a) and (b) show the *j*/*t* curves recorded for alloys I and II, respectively. Measurements were carried out in 0.5 M NaCl solution as a function of applied anodic potential (E_a: −0.2 to 0.5 V *vs.* SCE) at 25 °C.

Different *j*/*t* profiles that deserve comments were obtained depending upon the location of E_a *versus* E_b and the chemical composition of the tested alloy. When E_a is cathodic to E_b, the

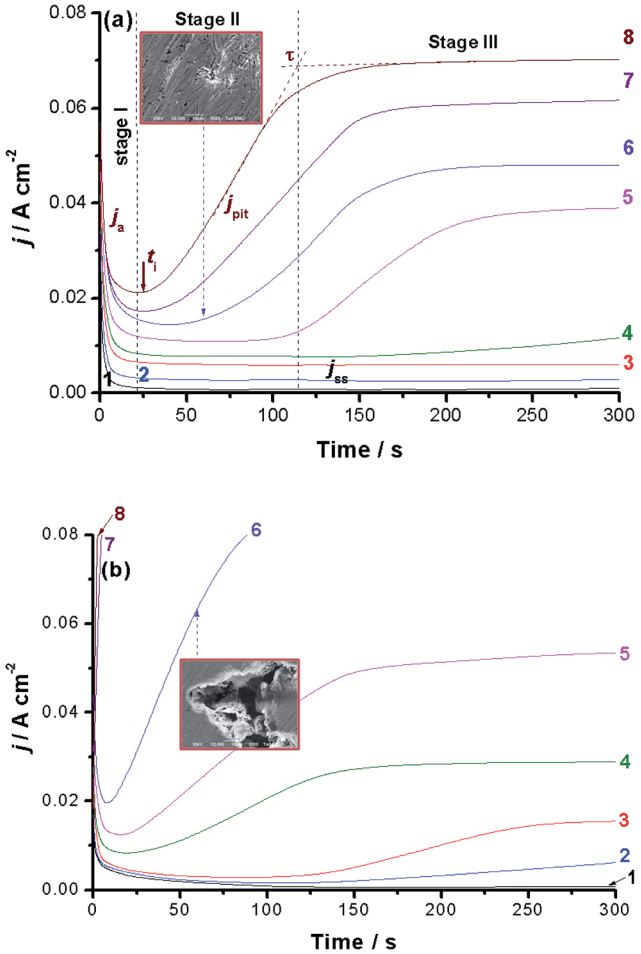

Fig. 2 Chronoamperometry measurements recorded for (a) alloy I (CoNiGa SMA) and (b) alloy II (CoNiGaAl SMA) in 0.5 M NaCl solutions at 25 °C as a function of the applied anodic potential (E_a). (1) −0.2 V(SCE); (2) −0.1 V(SCE); (3) 0.0 V(SCE); (4) +0.1 V(SCE); (5) +0.2 V(SCE); (6) +0.3 V(SCE); (7) +0.4 V(SCE); (8) +0.5 V(SCE). Insets: SEM images captured for the two alloys in 0.5 M NaCl solutions at 25 °C after holding the alloy at E_a = 0.3 V(SCE) for 60 s.

transient current profile can be divided into two stages, as shown for alloy I (Fig. 2(a), curves 1–3) and alloy II (Fig. 2(b), curve 1). In the first stage, the anodic current (j_a) first decreases as a result of the electroformation and growth of a passive oxide film on the anode surface. This decay in j_a varies, as will be shown later, according to the chemical composition of the tested alloy. Following this decay, j_a reaches a steady-state value, designated here as j_{ss} (related to j_{pass}), the current of the second stage. Once j_{ss} is attained and well-established, the rates of the passive layer growth and its dissolution are balanced, so that the oxide film hardly grows and a constant passive current results. Close inspection of Fig. 2 (also inspect ESI Fig. S5†) reveals that the rate of j_a decay, and hence the passivation rate, of alloy II, that is alloyed with Al, is higher than that of alloy I (the Al-free alloy). This indicates that alloy I tends to passivate in these solutions more effectively than alloy II. This in turn adds another evidence that Al when added to the CoNiGa SMA (alloy I) weakens its passivity making it less resistant to passivity breakdown and subsequent pitting attack.

Open Access Article. Published on 13 January 2017. Downloaded on 10/20/2025 1:41:01 AM. This article is licensed under a Creative Commons Attribution 3.0 Unported Licence.

Alloy I maintained its passive behavior even when E_a is approaching E_b. Only j_{ss} enhanced with E_a (Fig. 2(a), curves 1–4), denoting destabilization (oxide thinning/dissolution) of the passive oxide film as a result of the corrosive attack of Cl^- anions, but still passive within this period of time reflecting its high corrosion resistance. On the contrary, and within the same potential range, alloy II exhibited new curve features, as shown in Fig. 2(b) (curves 3 and 4). This curve feature can be classified into the three stages, namely stages I–III for passivation stage, pit formation and growth stage, and the final steady-state stage, respectively. The stage I's current falls with time, denoting the electroformation and growth of the passive layer. Then it reaches its minimum value, corresponding to the maximum thickness and protectiveness of the passive layer, at a certain time known as the incubation time (t_i); the time required for local removal of the passive film *via* the sequence of Cl^- adsorption, penetration and formation of soluble complexes.[29–32] It indicates the beginning of the pit nucleation period, where its magnitude reflects the susceptibility of the oxide film to breakdown.[30–33]

Stage II starts from t_i and ends at another time designated here as τ. The current of this stage, termed here as pit current j_{pit}, rises from the moment just after t_i till τ. The current growth within the 2nd stage suggests that pit formation and growth are the dominant processes. New pits may also develop following this active period, *i.e.*, t_i. Following the current rise between t_i and τ (*i.e.*, stage II), j_{pit} attains a steady-state, denoting stage III. This steady-state stage can be explained on the basis that pitting corrosion products formed during pit initiation and growth (stage II) precipitate inside the pits, blocking them up and therefore hinder the current flow (j_{pit}) through the pits. It is most probable that a steady-state is established between the metal dissolution and oxide film formation including a blockade by pitting corrosion products in stage III of current transient after τ. Similar findings were previously obtained in our lab during pitting corrosion studies of some metals and alloys.[38–41]

Alloy I showed the same trend but with much longer t_i and lower j_{pit} values than those of alloy II at the same E_a values, compare for example curves 5 and 6. Beyond E_b, alloy I exhibited no change in its passivation and pit formation and growth behavior (Fig. 2(a) curves 7 and 8), even the final steady-state current persists. However, alloy II (Fig. 2(b) curves 7 and 8 and ESI, Fig. S6†) showed that stage I (the first passivation stage) is disappeared and the current grows very rapidly and almost linearly immediately after switching the applied anodic potential, then it reaches steady-state. Further inspection of Fig. 2(a) and (b) reveals that j_{pit} enhances and t_i gets shorter, and hence increased pitting attack results, as E_a is made more anodic. At the same E_a, the values of j_{pit} are always smaller and those of t_i are longer for alloy I than alloy II. These findings again confirm the higher susceptibility of alloy II towards pitting as compared with alloy I. SEM examinations, images in the insets of Fig. 2(a) and (b), recorded for the surfaces of alloys I and II after holding the alloy at $E_a = 0.3$ V(SCE) for 60 s in the test solution came to the same conclusion. See how the surface of alloy II suffers from intense pitting attack much more than alloy I.

3.3. Catalysis applications for the HER

Cyclic polarization and chronoamperometry measurements confirmed the obvious activation of CoNiGa MSMA towards pitting corrosion, even at the rest potential (revisit the surface morphologies of Fig. S4, ESI†), by adding Al as an alloying element. This activation influence of alloyed Al encouraged us to test these materials as active cathode materials for the HER. We propose here that pitting corrosion may increase the specific surface area of the alloy surface and create on it new O_2-deficient (most probably due to thinning of the passive layer, depassivation, induced by adsorbed Cl^-) active sites capable of catalyzing the HER. This proposal is supported here from SEM/EDX mapping and XPS studies (see Section 3.4) and may require additional future investigations. In addition, and to the best of our knowledge, there are no reports in the literature regarding hydrogen generation over CoNiGa and CoNiGaAl MSMAs. For the above reasons, the HER performance of the two tested MSMAs, namely alloys I and II was studied, as shown in Fig. 3(a). The results performed on pure Co, pure Ni, $Co_{50}Ni_{50}$, and Pt/C cathodes were also included for comparison. Curves 5 and 7 represent the cathodic polarization curves recorded for alloys I and II, respectively, but after 24 h of immersion in 0.5 M NaCl solutions at room temperature. The aim, as will be shown later, is to access the role of surface roughness, resulted due to corrosion induced by the aggressive Cl^- anions, in improving the HER activity of the two tested SMAs.

The HER kinetics of the studied catalysts was probed by the corresponding η *vs.* $\log j$ plots, Fig. 3(b). The linear portions of these plots were fitted to the Tafel equation, expressed as shown in eqn (1):[42]

$$\eta = (2.3RT/n\alpha F)\log j_o - (2.3RT/n\alpha F)\log j \quad (1)$$

where, η is the cathodic overpotential, j_o is the exchange current density, n is the number of electrons involved in the electrode reaction, and α is the charge-transfer coefficient. The various electrochemical kinetic parameters associated with the HER were determined, Table 1. These include the Tafel slope (β_c), the over potentials at an apparent cathodic current density of 10 mA cm^{-2} (η_{10}) and the exchange current densities (j_o). Exchange current densities are referred to the geometric area of the electrodes, and were calculated *via* Tafel extrapolation till $\eta = 0$ (ESI, Fig. S7†).

Fig. 3(a) reveals that pure Co and Ni cathodes (curves 1 and 2) exhibit the worst catalytic activity towards the HER among the tested cathodes, as the proton reduction on their surfaces started at highly negative onset potentials, E_{HER}. Moreover, small cathodic currents were obtained beyond E_{HER}. The value of E_{HER} (−340 mV *vs.* RHE) recorded for the $Co_{50}Ni_{50}$ alloy (curve 3) is smaller, accompanied with higher cathodic currents, than those measured for Co (−385 mV *vs.* RHE) and Ni (−370 mV *vs.* RHE). Also, the value of j_o recorded for the $Co_{50}Ni_{50}$ alloy (3.4×10^{-3} mA cm^{-2}) is ~23 times greater than that measured for Co alone (1.5×10^{-4} mA cm^{-2}) and ~15 times that of Ni alone (2.3×10^{-4} mA cm^{-2}). These results demonstrate that the $Co_{50}Ni_{50}$ alloy exhibits higher catalytic

Open Access Article. Published on 13 January 2017. Downloaded on 10/20/2025 1:41:01 AM.
This article is licensed under a Creative Commons Attribution 3.0 Unported Licence.

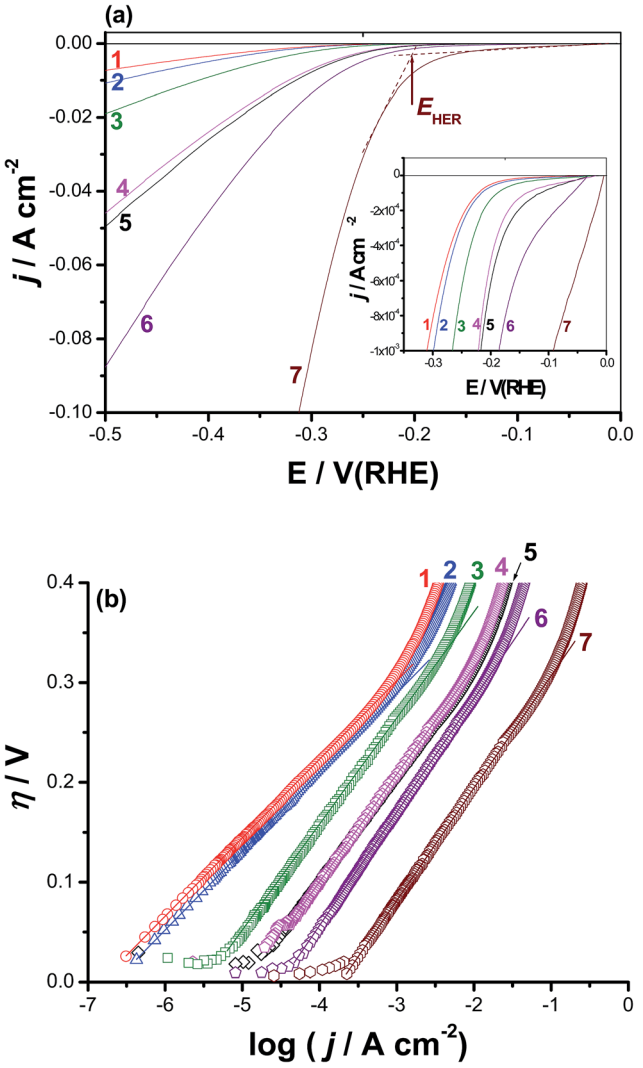

Fig. 3 Electrocatalytic hydrogen evolution of catalysts 1–7: (a) polarization curves for the HER on the surfaces of such catalysts. (b) Tafel plots for the tested catalysts derived from (a). Measurements were conducted in deaerated 0.1 M KOH aqueous solutions at a scan rate of 5 mV s^{-1} at 25 °C. (1) pure Co; (2) pure Ni; (3) $Co_{50}Ni_{50}$ alloy; (4) $Co_{50}Ni_{23}Ga_{27}$ (alloy I), (5) alloy I after 24 h of free corrosion in 0.5 M NaCl solution at 25 °C; (6) $Co_{50}Ni_{23}Ga_{26}Al_{1.0}$ (alloy II); (7) alloy II after 24 h of free corrosion in 0.5 M NaCl solution at 25 °C.

activity for the HER than Co and Ni alone, most probably as a consequence of the improvement in the intrinsic catalytic activity due to the synergetic effect of the two alloying metals.[43–47] Further improvement in the HER catalytic performance of the $Co_{50}Ni_{50}$ alloy (curve 3) has occurred upon alloying it with Ga at the expense of Ni to yield the $Co_{50}Ni_{23}Ga_{27}$ MSMA (alloy I), curve 4, reflecting the catalytic impact of alloyed Ga. This is clear from Table 1 where alloy I recorded a j_o value of 0.011 mA cm^{-2}, which is 3.2 times grater than that calculated for $Co_{50}Ni_{50}$ alloy (3.4×10^{-3} mA cm^{-2}).

The addition of a small amount of alloyed Al (1.0%) to alloy I at the expense of Ga to yield alloy II ($Co_{50}Ni_{23}Ga_{26}Al_{1.0}$) has markedly enhanced the HER activity, denoting the important role the alloyed Al play in catalyzing the HER. In this respect, the value of E_{HER} has decreased, as shown in Table 1, from −295 mV *vs.* RHE for alloy I to −250 mV *vs.* RHE for alloy II, and the cathodic polarization curves get much more steeper (*i.e.*, higher cathodic currents and increased kinetics for the HER) in presence of alloyed Al (compare between curves 3 and 4). In addition, the value of j_o measured for alloy II (0.04 mA cm^{-2}) is found to be ∼4 times higher than that of alloy I (0.011 mA cm^{-2}).

The overpotential (η_{10}) requires to achieve a current density of 10 mA cm^{-2} is also considered an important controlling parameter for the apparent electrode activity for the HER.[48–50] Data of Table 1 infer that the values of η_{10} decrease, and hence accelerated kinetics of the HER is achieved, following the sequence: Co < Ni < $Co_{50}Ni_{50}$ < alloy I < alloy II.

It is worth mention here that the j_o value of alloy I is doubled and that of alloy II has increased 5 times, approaching that of Pt/C under the same experimental conditions (∼0.7 mA cm^2 (ref. 51)) when the two alloys are subjected to a corrosion process (24 h of free corrosion in 0.5 M NaCl solution at 25 °C) prior to performing the cathodic polarization measurements. These results refer, for the first time, to the catalytic impact of corrosion, which is a well-known destructive process. This undesirable process can therefore be used to produce useful materials for wide applications, such as electrocatalysts here.

The HER proceeds in the alkaline solutions following either Volmer–Heyrovsky or Volmer–Tafel mechanisms:[51,52]

Volmer step:

$$H_2O + e^- + S^* \leftrightarrow H_{ads} + OH^- \quad (2)$$

Heyrovsky step:

$$H_{ads} + H_2O + e^- \leftrightarrow H_2 + OH^- + S^* \quad (3)$$

Tafel step:

Table 1 Mean value (standard deviation) of the electrochemical kinetic parameters for the HER on the surfaces of alloys I and II in 0.1 M KOH solution at 25 °C, in a comparison with those recorded for Co, Ni, NiCo, and Pt/C electrodes

Tested cathode	E_{HER}/mV(RHE)	$-\beta_c$/mV dec^{-1}	j_o/mA cm^{-2}	η_{10}/mV
Pure Co	−385(8)	82(2.05)	$1.5(0.1) \times 10^{-4}$	382(9)
Pure Ni	−370(7)	80(1.6)	$2.3(0.05) \times 10^{-4}$	371(7)
$Co_{50}Ni_{50}$ alloy	−340(7)	105(2.3)	$3.4(0.07) \times 10^{-3}$	364(6)
Alloy I (NiCoGa)	−295(6)	109(2.5)	0.011(0.002)	320(5)
Alloy I after 24 h of immersion in 0.5 M NaCl at 25 °C	−284(6)	107(1.5)	0.0124(0.002)	313(4.5)
Alloy II (NiCoGaAl)	−250(5)	115(1.9)	0.04(0.003)	285(4.8)
Alloy II after 24 h of immersion in 0.5 M NaCl at 25 °C	−220(5)	113(1.7)	0.2(0.025)	194(4.3)

Open Access Article. Published on 13 January 2017. Downloaded on 10/20/2025 1:41:01 AM.
This article is licensed under a Creative Commons Attribution 3.0 Unported Licence.

$$2H_{ads} \leftrightarrow H_2 + S^* + S^* \quad (4)$$

where S* refers to an active adsorption site for hydrogen. Durst *et al.*[52] studied the electrochemical hydrogen oxidation and evolution reaction mechanism on Pt/C in alkaline solutions and reported that the Volmer step, with a Tafel slope ~120 mV dec^{-1}, is the rate-limiting step for the HER on Pt/C.[51,52] From Table 1, alloys I and II (without and with corrosion pretreatment) exhibit Tafel slope values of 109, 107, 115, and 113 mV dec^{-1}, respectively. These values of Tafel slopes are close to that measured on Pt/C (111 mV dec^{-1}) in the same alkaline solution (0.1 M KOH),[51,52] suggesting that the HER kinetics of alloys I and II is similar to that of Pt/C.

Impedance measurements were also carried out at selected cathodic overpotentials, namely −0.3, −0.5, and −0.7 V *vs.* RHE to further clarify the activation influence of alloyed Al on the kinetics of the HER. Fig. 4 represents the electrochemical impedance spectra in the complex plane recorded at −0.5 V *vs.* RHE. The impedance behaviour of pure Co, pure Ni, CoNi, and Pt/C electrodes were also included in Fig. 4 for comparison. The obtained complex plane impedance spectra of all studied catalysts (except for Pt/C, which displayed a single capacitive loop) exhibit two well-defined depressed semicircles (two time constants). Similar results were obtained at −0.3 and −0.7 V *vs.* RHE (their plots are not included, but their fitting results are reported and discussed here, see Table 2). Such impedance responses are commonly obtained for electrocatalytic evolution of hydrogen on Ni,[53] Co,[54] and some of their alloys[43–45,55] in alkaline solutions. Also, similar impedance profiles were previously obtained in our lab during catalytic HER studies in H_2SO_4 solutions on reduced graphene oxide nanosheets and titanium substrates decorated by some metallic nanoparticles.[56–58]

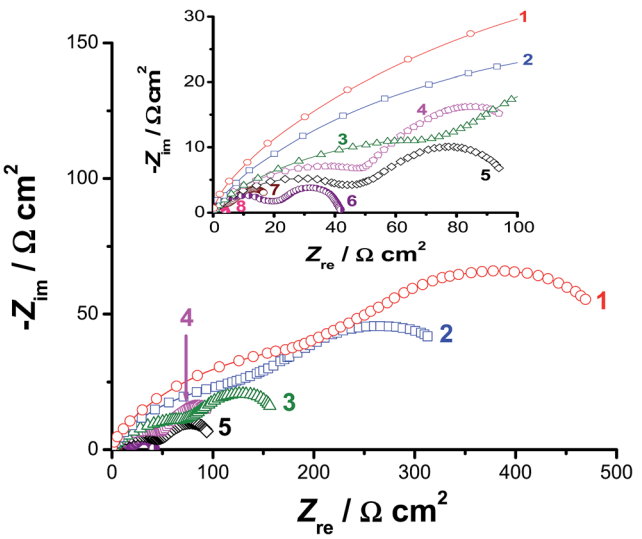

Fig. 4 Complex-plane impedance plots recorded for the studied catalysts in deaerated 0.1 M KOH aqueous solutions at a cathodic overpotential of −0.5 V *vs.* RHE at 25 °C. (1) Pure Co; (2) pure Ni; (3) $Co_{50}Ni_{50}$ alloy; (4) $Co_{50}Ni_{23}Ga_{27}$ (alloy I), (5) alloy I after 24 h of free corrosion in 0.5 M NaCl solution at 25 °C; (6) $Co_{50}Ni_{23}Ga_{26}Al_{1.0}$ (alloy II); (7) alloy II after 24 h of free corrosion in 0.5 M NaCl solution; (8) Pt/C catalyst.

The first semicircle (with diameter R_1) was observed at high frequencies, while the second one (the diameter of which is R_2) was formed at the low frequency values. Each of them can be assigned to the resistance–capacitance (*RC*) network. Each *RC* network consists of the charge-transfer resistance (R_1 for the first semicircle and R_2 for the second one) of the H^+ reduction process and the corresponding double-layer capacitance (C_1 for the first semicircle and C_2 for the second one) at the catalyst/electrolyte interface. The total charge-transfer resistance (R_{ct}) equals the summation of R_1 and R_2. To calculate the elements of such *RC* networks, and hence gain more insight into the HER kinetics associated with EIS measurements, the experimental impedance data were fitted using the equivalent circuit presented and fully described elsewhere.[58] The obtained fitting parameters are presented in Table 2 as a function of the applied cathodic overpotentials. It follows from Table 2 that, for any tested catalyst, the values of R_1 and R_2 decrease as the applied cathodic overpotential made more negative, referring to enhanced HER kinetics. These results infer that the total impedance of the studied interfaces is associated to the HER kinetics.

Data of Table 2 reveal that the value of R_{ct}, at any given applied potential, is smaller (*i.e.*, accelerated HER kinetics) for alloy II (that is alloyed with Al) than those measured for the other studied catalysts. For instance, alloy II recorded an R_{ct} value of 41 Ω cm^2@−0.5 V(RHE), which is the smallest among the others (Table 2: R_{ct} = 694, 472, 218, and 130 Ω cm^2 for Co, Ni, CoNi, and alloy I, respectively) at the same overpotential. These findings support the catalytic influence of the alloyed Al. The R_{ct} value of alloy II is diminished (*i.e.*, faster and faster HER kinetics is achieved) from 41 Ω cm^2@−0.5 V(RHE) to 21.5 Ω cm^2 at the same overpotential after modifying its surface *via* the corrosion pretreatment process, approaching that of the commercial Pt/C catalyst (4.3 Ω cm^2). These results confirm the high HER catalytic performance of the corroded surface of alloy II, highlighting again the catalytic impact of corrosion.

Further inspection of Table 2 reveals that, at any given potential, the largest capacitance (*Q* and *C*) value was recorded for alloy II after being activated by pitting corrosion, referring to its large active surface area. This increased active surface area of the pitted surface of alloy II promotes HER catalytic performance of the alloy. To confirm these findings, the electrochemical active surface area (EASA) of the studied catalysts was estimated. There are a number of different techniques described in literature for EASA measurements. One estimation procedure involves calculation of the roughness factor (R_f) from EIS data, more precisely from estimated double layer capacitance values.[59,60] We considered here the values of *Q* rather than those of *C* for the calculation of R_f, as the former (Q, where $Q = R_{ct}^{-1}(C \times R_{ct})^n$) provides more information about surface inhomogeneity and roughness,[61,62] and also includes the parameter *n*, which is also related to surface roughness.[63,64] For a typical smooth surface, $n = 1$ and $C = 20$ μF cm^{-2}.[59,60] This gives a value of 20 S^n (ω^{-1} cm^{-2}) for $Q_{calculated}$. The obtained R_f values ($R_f = Q_{measured}/Q_{calculated}$; $Q_{measured} = Q_1 + Q_2$) are shown in Table S3 (ESI†) for each studied catalyst as a function of the applied cathodic potential. Table S3† revealed that, for any

Open Access Article. Published on 13 January 2017. Downloaded on 10/20/2025 1:41:01 AM.
This article is licensed under a Creative Commons Attribution 3.0 Unported Licence.

Table 2 Mean value (standard deviation) of the impedance parameters recorded for the studied catalysts. Measurements were conducted in 0.1 M KOH solutions at cathodic potentials −0.3, −0.5, and −0.7 V *vs.* SCE at 25 °C

Catalyst	E (V(RHE))	Q_1 (S^n (ω^{-1} cm^{-2}))	R_1 (Ω cm^2)	n_1	C_1 (μF cm^{-2})	Q_2 (S^n (ω^{-1} cm^{-2}))	R_2 (Ω cm^2)	n_2	C_2 (μF cm^{-2})	R_{ct} (Ω cm^2)
Co	−0.3	22.1(0.4)	426(7)	0.94	16.4(0.24)	19(0.4)	457(7.8)	0.95	14.8(0.22)	883(14.8)
	−0.5	28.2(0.5)	308(5)	0.93	19.7(0.29)	28.1(0.5)	386(6.2)	0.92	19(0.28)	694(11.2)
	−0.7	36.6(0.7)	223(4)	0.91	22.8(0.34)	34.6(0.6)	291(5.4)	0.90	20.8(0.31)	514(9.4)
Ni	−0.3	26.1(0.5)	388(5.4)	0.93	18.5(0.27)	24.4(0.4)	405(5.8)	0.94	18.2(0.27)	793(11.2)
	−0.5	35.6(0.7)	206(3.1)	0.93	24.6(0.36)	35.5(0.7)	266(4.2)	0.92	23.7(0.34)	472(7.3)
	−0.7	47.3(0.9)	102(2)	0.91	27.9(0.41)	44.7(0.8)	128(2.3)	0.91	26.8(0.4)	230(4.3)
$Co_{50}Ni_{50}$	−0.3	43.6(0.8)	247(3.6)	0.89	24.9(0.37)	37.9(0.7)	279(4.2)	0.91	24.2(0.33)	526(7.8)
	−0.5	55.6(1.1)	108(2.2)	0.88	27.7(0.42)	52.3(1.05)	110(2.4)	0.89	27.6(0.41)	218(4.6)
	−0.7	76.1(1.5)	63(1.2)	0.86	31.9(0.47)	69.5(1.39)	69(1.4)	0.87	31.3(0.45)	132(2.6)
Alloy I (without corrosion pretreatment)	−0.3	52(1.05)	133(2.3)	0.88	26.4(0.39)	45.1(0.9)	145(2.6)	0.90	25.8(0.38)	278(4.9)
	−0.5	79.4(1.6)	68(1.2)	0.85	31.6(0.47)	68.6(1.37)	62(1.3)	0.88	32.6(0.49)	130(2.5)
	−0.7	109.8(2.2)	44(0.8)	0.84	39.8(0.6)	89.6(1.8)	47(0.9)	0.87	39.6(0.58)	91(1.7)
Alloy I (after corrosion pretreatment)	−0.3	60.5(1.2)	122(2.2)	0.86	27.2(0.41)	58.4(1.17)	133(2.6)	0.88	26.5(0.39)	255(4.8)
	−0.5	86.8(1.7)	52(1.02)	0.85	33.4(0.5)	80.4(1.61)	55(1.1)	0.86	33.2(0.49)	107(2.12)
	−0.7	127.1(2.5)	38(0.7)	0.83	42.7(0.64)	109.5(2.2)	41(0.8)	0.85	42.2(0.63)	79(1.5)
Alloy II (without corrosion pretreatment)	−0.3	85.3(1.7)	56(1.1)	0.85	33.2(0.5)	75(1.5)	68(1.3)	0.86	31.7(0.47)	124(2.4)
	−0.5	148.9(2.9)	19(0.33)	0.84	48.7(0.73)	133.5(2.7)	22(0.4)	0.85	47.9(0.71)	41(0.73)
	−0.7	208.1(4.1)	11(0.2)	0.82	54.8(0.82)	178.9(3.6)	15(0.32)	0.83	53.2(0.79)	26(0.52)
Alloy II (after corrosion pretreatment)	−0.3	177.1(3.5)	15.6(0.3)	0.83	53(0.8)	134.9(2.7)	28.8(0.6)	0.84	46.8(0.7)	44.4(0.9)
	−0.5	382.8(7.7)	5.4(0.11)	0.81	89.8(1.3)	175.9(3.5)	16.1(0.3)	0.83	52.9(0.79)	21.5(0.41)
	−0.7	832.9(14.6)	2.6(0.05)	0.78	147.6(2.2)	347.8(7.2)	7.2(0.14)	0.80	77.8(1.17)	9.8(0.19)

studied catalyst, R_f increases as the applied potential is made more cathodic, where H_2 evolves progressively and can incorporate in the crystal lattice of the investigated cathode. This in turn may create voids and flaws, resulting in increased surface roughness.[65–67] This effect is quite clear in case of alloy II, particularly after the corrosion pretreatment process, where R_f varied markedly with potential (R_f = 15.6, 27.94, and 59.04 at −0.3, −0.5, and −0.7 V *vs.* RHE, respectively). In the absence of the corrosion pre-treatment process, the value of R_f at any given potential is doubled when we go from alloy I (for instance, R_f = 9.97@−0.7 V *vs.* SCE) to alloy II (R_f = 19.35 at the same potential) thus, confirming the catalytic impact of alloyed Al. The accelerating influence of pitting corrosion is also clear from Table S3;† the pitted surface of alloy II (the best catalyst here) recorded an R_f value of 59.04 at −0.7 V *vs.* SCE, which is 3 times greater than that measured for the non-pitted surface of the same alloy at the same potential (R_f = 19.35). Therefore, the values of R_f clearly indicate (in accordance with SEM images) development of surface area.

The faradaic efficiency (FE) of the HER was also determined for alloys I and II without and with the corrosion pretreatment process, see Table 3, to further evaluate their electrocatalytic performance and support electrochemical findings. This was achieved *via* dividing the experimentally measured volume of H_2 by its theoretical volume (the procedure is reported in more details in the ESI,† Section 1). Fig. 5 shows the comparison of the theoretical volume of H_2 and its experimentally measured volume for the best catalyst, namely the pitted surface of alloy II which produced *via* dipping alloy II (as-polished) in 0.5 M NaCl for 24 h at 25 °C. Similar results were obtained for Pt/C and the other tested catalysts (ESI, Fig. S8†). The charge *vs.* time plots obtained for the studied catalysts during 1 h of a controlled

Table 3 Mean value (standard deviation) of the amounts of hydrogen (measured and calculated) per hour by a controlled potential electrolysis process[a] and the faradaic efficiency values, FE (%), for alloys I and II without and with corrosion pretreatment[b]

Catalyst	H_2 measured by gas chromatography (H_2/μmol h^{-1})	Calculated H_2 based on the charge passed during electrolysis		FE (%)
		Charge passed/C	H_2/μmol h^{-1}	
Alloy I (without corrosion pretreatment)	6.5(0.1)	1.66(0.023)	8.6(0.12)	75.6(0.11)
Alloy I (with corrosion pretreatment)	7.3(0.11)	1.8(0.03)	9.3(0.16)	78.5(0.17)
Alloy II (without corrosion pretreatment)	11.8(0.18)	2.58(0.038)	13.4(0.2)	88.06(0.03)
Alloy II (with corrosion pretreatment)	18(0.26)	3.6(0.05)	18.7(0.26)	96.3(0.07)
Pt/C	20.5(0.28)	3.98(0.06)	20.6(0.32)	99.5(0.18)

[a] A chronoamperometry run where the catalyst is held at −0.8 V *vs.* RHE for 1 h in 0.1 M KOH solution at 25 °C. [b] Prior to performing the chronoamperometry experiment, the electrode is first subjected to 24 h of free corrosion in 0.5 M NaCl solution at 25 °C.

Open Access Article. Published on 13 January 2017. Downloaded on 10/20/2025 1:41:01 AM.
This article is licensed under a Creative Commons Attribution 3.0 Unported Licence.

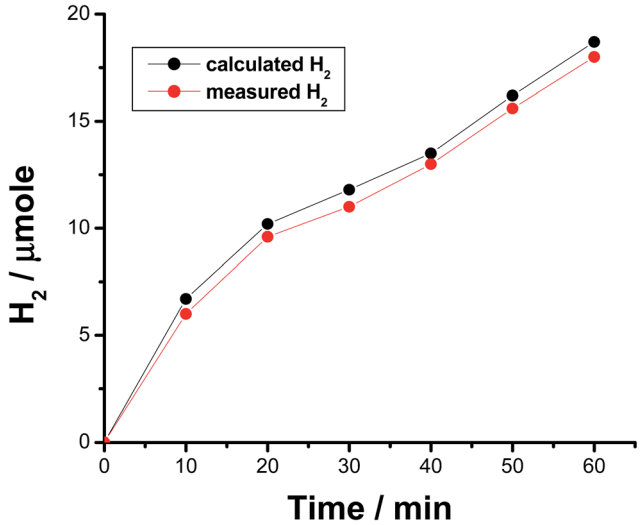

Fig. 5 Volume of H_2 calculated from the amount of charge passed (assuming 100% faradaic efficiency) and that of H_2 measured from gas chromatography during 1 h of a controlled potential electrolysis run of the best catalyst (the pitted surface of alloy II) at −0.8 V *vs.* RHE in 0.1 M KOH aqueous solution.

potential electrolysis process (a potentiostatic experiment where the tested catalyst was held at −0.8 V *vs.* RHE for 1 h in a 0.1 M KOH solution) are depicted in Fig. 6 in a comparison with Pt/C. Here again, as shown in Table 3, the experimentally measured volume of H_2 produced by alloy II (11.8 μmol h^{-1}, with a corresponding FE of 88%) is higher than that yielded by alloy I (7.3 μmol h^{-1}, FE 75.6%), confirming the catalytic impact of alloyed Al. The catalytic influence of corrosion is also evident from Table 3. Alloy II, after being modified by the corrosion pretreatment process, produced 18 μmol h^{-1} of H_2 (FE 96%, approaching that of Pt/C, ∼100%), which is 1.5 times greater than that recorded by the same alloy but without corrosion pretreatment (11.8 μmol h^{-1}, FE 88%). That means 96% of the electrical charge that passes through the system was consumed for the HER. The rest of charge may be wasted in some parasitic electrochemical processes simultaneously occurring during the HER. These may be reduction of dissolved O_2 and, although less common, metal ion reduction and metal deposition. O_2 reduction is most probably excluded as the test solution was deaerated and the cell sealed, unless traces of O_2 still exist in solution. Pt is used here as the counter electrode, and dissolution of minute amounts of Pt and its re-deposition at the cathode may occur, consuming part of electricity. This in turn may help improve the catalytic properties of the tested cathode. To exclude or ensure this possibility, a carbon electrode was used as the anode instead of Pt, and the same catalytic activity was obtained. Cathodic corrosion may also occur as a result of H_2 incorporation in the cathode's crystal lattice, particular Ni during electrolysis,[65–67] but ICP-AES did not detect any cations in solution after electrolysis. Perhaps once formed in minute amounts, metal ions (released from the cathode) in solution re-deposited during electrolysis and this may also consume part of electricity.

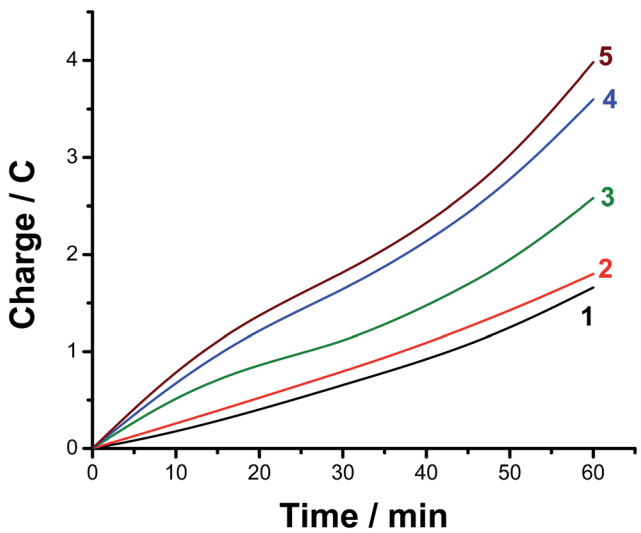

Fig. 6 Charge *vs.* time plots of alloys I and II without and with corrosion pre-treatment, in a comparison with Pt/C, during 1 h of a controlled potential electrolysis process at −0.8 V *vs.* RHE in 0.1 M KOH aqueous solution. (1) Alloy I (without corrosion pre-treatment); (2) alloy I (with corrosion pre-treatment); (3) alloy II (without corrosion pre-treatment); (4) alloy II (with corrosion pre-treatment); (5) Pt/C.

The above findings indicated that the investigated CoNiGaAl after pitting corrosion process is catalytically active for the HER. This high HER catalytic activity of the pitted surface of alloy II is found to be comparable, and even higher than that of other recently reported active Co- and Ni-based electrocatalysts.[43–47,68–73]

The activation influence of alloyed Al towards pitting attack and its catalytic impact on the kinetics of the HER on alloy II are evident from the above findings and deserves interpretation, *vide infra*.

3.4. Origin of catalytic activity

3.4.1. Catalysis due to alloyed Al. The role played by alloyed Al in activating the alloy surface for both pitting corrosion and the HER can be explained on the basis of microstructure study, Fig. 7. It is seen that the microstructure of both alloys consists of γ phase, with high Co content, as a trunk phase in addition to a Ga rich martensite phase. The volume fraction (V_f) of the martensite phase in the CoNiGa alloy (image (a)) is markedly increased by the addition of 1 at% Al at the expense of that of the γ phase, as shown in image (b). This was confirmed from EDX analysis of such phases (ESI, Table S4†), where V_f of the γ phase represented 42.56% of the microstructure of CoNiGa alloy, and decreased to 37.44% by the addition of 1 at% of Al.

It is well known that the γ phase has higher corrosion resistance than martensite phase. In this respect, the effect of martensite phase on decreasing corrosion resistance of stainless steel has been reported.[74–76] Based on these considerations, the low corrosion resistance and high HER catalytic activity of alloy II can be attributed to the high V_f of the martensite phase in its microstructure, image (b), as compared with alloy I (that with low V_f of the martensite phase, image (a)). Moreover, the particle size of the γ phase in CoNiGaAl alloy is much smaller than that of the same phase in CoNiGa alloy. Hence, the grain

 This journal is © The Royal Society of Chemistry 2017

Open Access Article. Published on 13 January 2017. Downloaded on 10/20/2025 1:41:01 AM.
This article is licensed under a Creative Commons Attribution 3.0 Unported Licence.

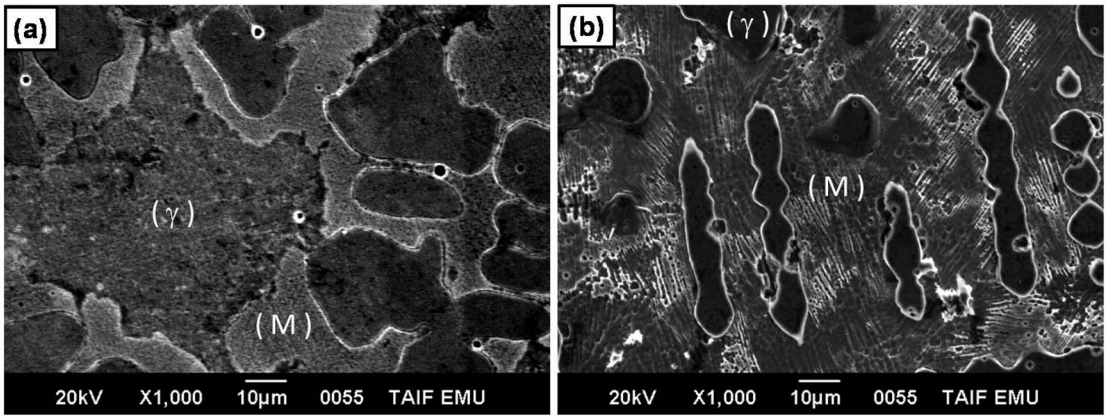

Fig. 7 Microstructure of CoNiGa (a) and CoNiGaAl (b) alloys.

Table 4 Binding energies and contribution (atomic%) of core levels: Co2p3, Ni2p3, Ga3d5, Cl2p3 and O1s elements present on the surface of CoNiGa and CoNiGaAl alloys before and after exposure to 0.5 M NaCl solution

	Co(1)	Co(2)	Ni(1)	Ni(2)	Ga(1)	Ga(2)	O(1)	O(2)	Cl
BE [eV]	778.4	782.0	853.0	854.2	18.6	20.3	531.0	532.4	200.3
CoNiGa_ref	50.0	0.9	23.5	2.4	14.3	1.6	4.3	3.0	—
CoNiGa_24 h	37.4	1.0	19.2	2.9	6.6	7.0	14.0	11.9	—
CoNiGaAl_ref	44.7	1.2	22.5	2.5	13.3	3.1	7.1	5.6	—
CoNiGaAl_24 h	17.7	2.0	8.9	2.9	6.1	3.9	12.7	23.6	22.2

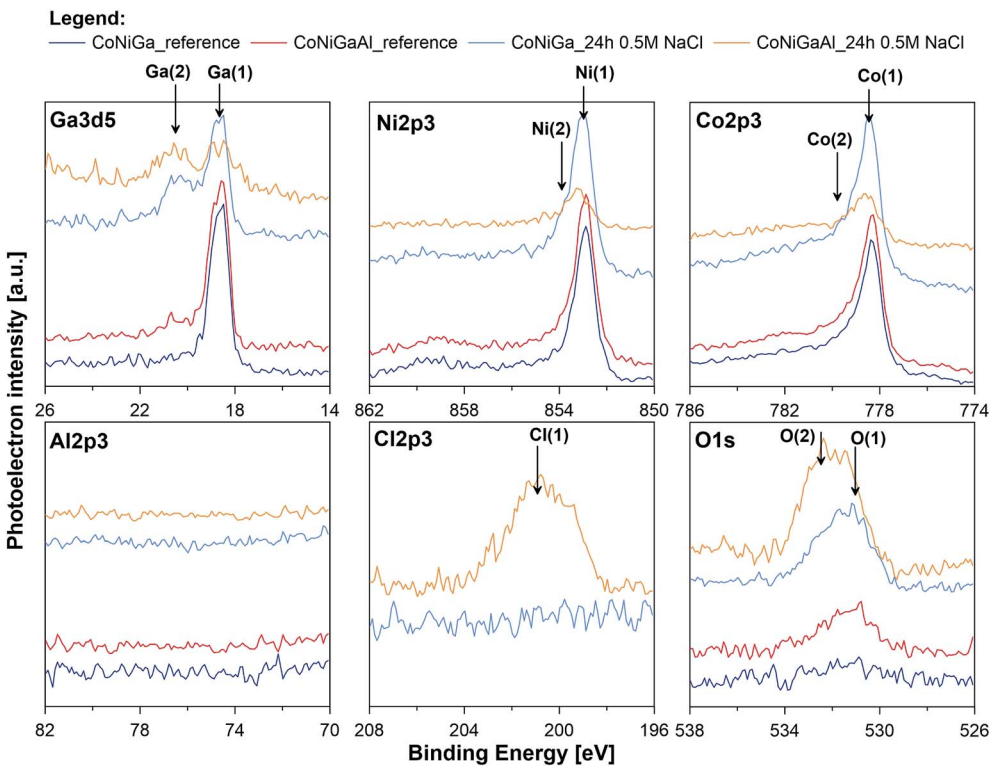

Fig. 8 High resolution XPS spectra recorded at gallium, nickel, cobalt, aluminium, chlorine and oxygen for CoNiGa and CoNiGaAl samples before and after 24 h immersion in naturally aerated 0.5 M NaCl.

boundary area in CoNiGaAl alloy is higher than in CoNiGa alloy. The area of the grain boundaries represent the imperfection in the polycrystalline alloys, therefore the candidate areas to be corroded are higher in CoNiGaAl than in CoNiGa alloy leading to higher corrosion rate in the former alloy than in the latter one. Such regions of imperfections may also catalyze the HER.

In an attempt to further assess the pitting corrosion activation influence of alloyed Al and its catalytic impact towards the HER, high resolution XPS study was performed for both investigated alloys before and after exposition in naturally aerated 0.5 M NaCl solution for period of 24 h (_ref and _24 h suffix in Table 4, respectively). Examination was carried out in the binding energy (BE) range of Ga3d5, Ni2p3, Co2p3, Al2p3, Cl2p3

Open Access Article. Published on 13 January 2017. Downloaded on 10/20/2025 1:41:01 AM.
This article is licensed under a Creative Commons Attribution 3.0 Unported Licence.

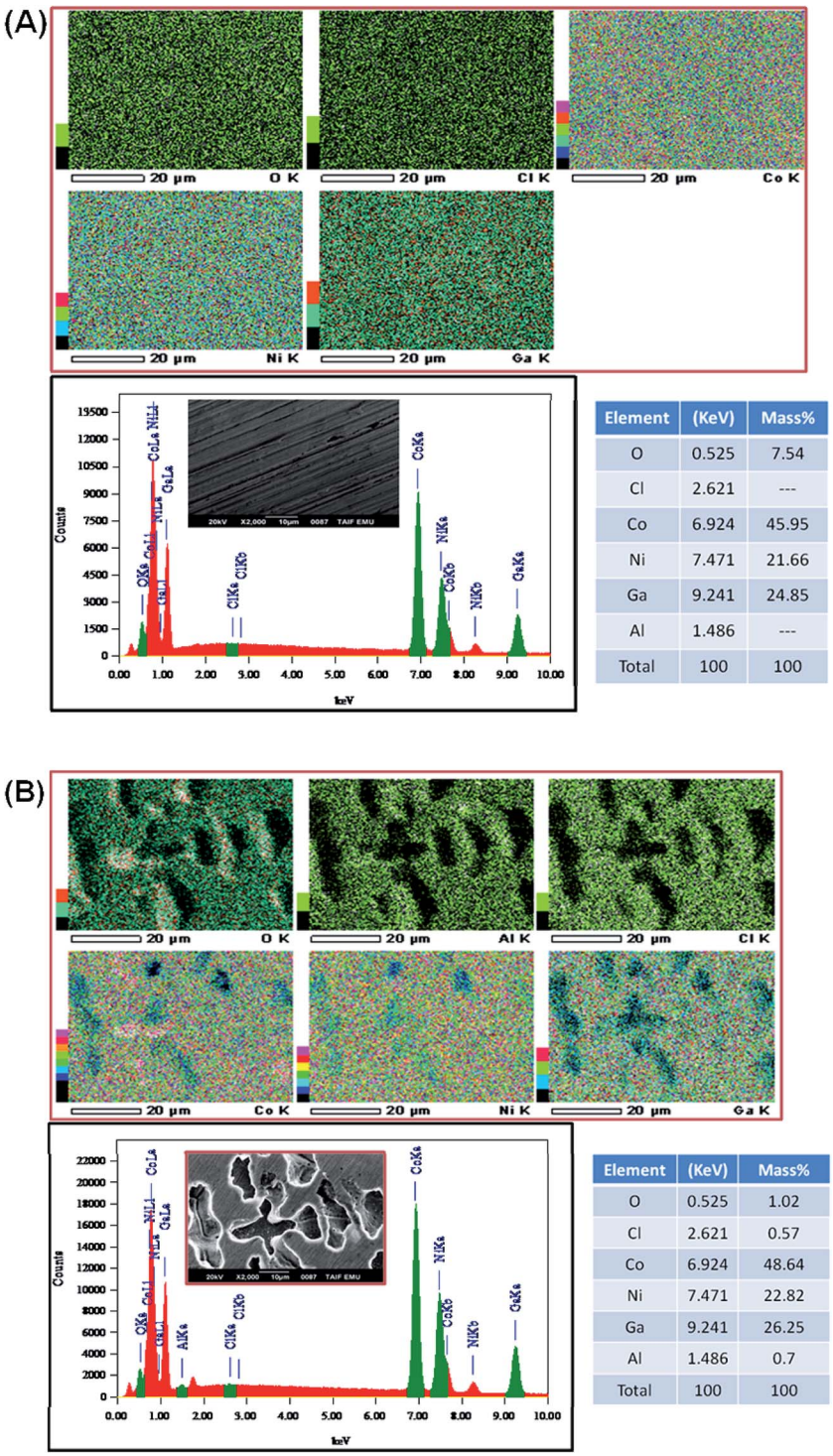

Element	(KeV)	Mass%
O	0.525	7.54
Cl	2.621	---
Co	6.924	45.95
Ni	7.471	21.66
Ga	9.241	24.85
Al	1.486	---
Total	100	100

Element	(KeV)	Mass%
O	0.525	1.02
Cl	2.621	0.57
Co	6.924	48.64
Ni	7.471	22.82
Ga	9.241	26.25
Al	1.486	0.7
Total	100	100

Fig. 9 SEM micrographs and corresponding EDX chemical maps acquired for the alloying elements (Co, Ni, Ga, and Al), in addition to the EDX chemical analysis for Cl and O, recorded for alloys I and II after 24 h of free corrosion in 0.5 M NaCl solutions at 25 °C.

Open Access Article. Published on 13 January 2017. Downloaded on 10/20/2025 1:41:01 AM.
This article is licensed under a Creative Commons Attribution 3.0 Unported Licence.

and O1s peaks and corresponding XPS spectra are presented on Fig. 8. Before XPS examination ion gun etching was performed for each investigated sample (1000 V, 100 s). Its purpose was to remove carbon and oxygen contamination due to exposure in atmospheric air.

The most dominant component was observed for Ga, Ni and Co in the energy range corresponding to chemical state of metal.[77] A very small signal from non-metallic compounds was also present in the form of metal oxides (Ga(2), Ni(2), Co(2)) that originates from thin passive layer formed spontaneously when samples were exposed to atmospheric air.[17] A well resolved Co2p and Ni2p spectra for metal shows complex structure. Asymmetric peaks were used during fitting procedure due to the presence of loss features and satellites.[78] No visible peak was detected in the energy range of Al2p peak doublet for neither sample (reference or after the exposure). Authors suggest that the amount of aluminium in alloy is below the threshold of its identification, EDX studies indicate share of aluminium below 0.8 mass% (Fig. 9). Characteristic values of peak BE were presented in Table 4.

Surface chemistry of investigated alloys change significantly as a result of 24 h exposition in naturally aerated 0.5 M NaCl. Gallium, which is next to Al, is the most active metal among the alloying components (−0.56 V compared to −0.28 V for Co and −0.24 V for Ni), oxidizes the most as a result of exposition. It can be seen, that surface coverage by gallium oxides is particularly significant for CoNiGa samples where Ga(1)/Ga(2) ratio drops from 8.9 merely to 0.9. In comparison, CoNiGaAl sample show decrease from 4.3 to 1.6. Second evident effect of sample exposure to 0.5 M NaCl is the appearance of Cl2p3 peak, manifesting itself in the energy range for metal chlorides, but only on CoNiGaAl alloy. Its share is above 20 at%. This high value may only indicate breakdown of the passive state combined with promotion of local corrosion of investigated alloy. The appearance of chlorides hinders Co(1), Ni(1) and Ga(1) peaks, which is to be expected. Considering the O1s spectra, the peak O(2) at 532.4 eV corresponding to hydroxide bonds is the main chemical state of oxygen for CoNiGaAl sample after exposure in NaCl. But for electrolyte-exposed CoNiGa samples O(1) peak at 531.0 eV is more pronounced, which indicates a higher fraction of oxidic bonding states and possibly a more stable passive state.[77] This chemical state is also apparent in the residual peaks registered for pre-exposed samples.

The XPS examinations confirm the conclusions drawn on the base of electrochemical and microstructure studies. The passive state is significantly weaker due to Cl adsorption on aluminium-containing alloy (alloy II) and lower presence of gallium oxide in the passive layer. This weak passive state of alloy II may create active adsorption sites for the reduction of H^+ on alloy II's surface, thus catalyzing the HER. This adds another reason behind the increased HER activity of alloy II as compared with alloy I; the later is characterized by stable passivity.

3.4.2. Catalysis due to pitting corrosion. SEM/EDX mapping study was also carried out to get an insight into the catalytic impact of pitting corrosion towards the HER. The SEM micrographs and corresponding EDX chemical maps acquired for the alloying elements, namely Co, Ni, Ga, and Al recorded for alloys I and II after 24 h of free corrosion in 0.5 M NaCl solutions at 25 °C are shown in Fig. 9. EDX chemical analysis for Cl and O were also included in Fig. 9. Like XPS, EDX analysis detected a considerable amount of adsorbed Cl on alloy II and no Cl on alloy I. This result supports Cl adsorption catalyzed by alloyed Al; another evidence for pitting corrosion catalysis by Al. This is the reason why alloy II suffers from intense pitting attack (Fig. 9(B), inset of the EDX spectra), while alloy I is immune to pitting, as shown in the inset of EDX spectra of Fig. 9(A). Some heterogeneity can be seen on EDX maps on CoNiGaAl samples due to such intense pitting attack. Surface roughness (due to pitting corrosion), and hence increased electrochemical active surface area, of alloy II is another important factor behind its high HER activity. In addition, further inspection of the EDX maps on CoNiGaAl sample reveals an obvious deficiency of oxygen, *i.e.*, weak passivity, inside pits. This in turn makes the walls of the pits active for the HER. The edges of these active pits may also contribute in catalyzing the HER.

3.5. Catalyst stability and durability

Catalyst's stability and durability are highly important criteria to evaluate its catalytic performance. Stability and long-term durability of the best catalyst was evaluated here by means of repetitive cycling (3000 cycles) of the cathodic polarization curves starting from E_{corr} up to a cathodic potential of −1.0 V(RHE), Fig. 10, and electrolysis at a high constant cathodic current density of 100 mA cm^{-2} for 24 h, see the inset of Fig. 10. It follows from Fig. 10 that the cathode exhibits excellent stability after 3000 times of continuous cycling up to a cathodic potential of −0.3 V *vs.* RHE. Beyond −0.3 V, it showed a slight degradation (due to small loss in the cathodic current density), which slightly enhances as the potential made more negative,

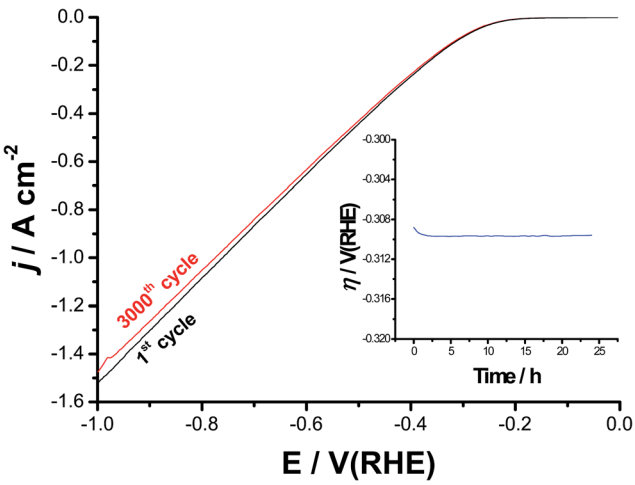

Fig. 10 Long-term stability and durability tests for the best catalyst (alloy II after 24 h of free corrosion in 0.5 M NaCl solution at 25 °C). Measurements were carried out in 0.1 M KOH solutions at 25 °C. The main figure represents the cathodic polarization curves initially and after 3000 of continuous cycles between −1.0 V(RHE) and E_{corr} at a scan rate of 50 mV s^{-1}. Inset: time-dependent overpotential curve at a constant cathodic current density of 100 mA cm^{-2} for 24 h.

Open Access Article. Published on 13 January 2017. Downloaded on 10/20/2025 1:41:01 AM.
This article is licensed under a Creative Commons Attribution 3.0 Unported Licence.

most probably due to accumulation of the H_2 bubbles at high cathodic potentials. This accumulated H_2 bubbles may cause some sort of catalyst deactivation.[79] In addition, a stable time-dependent overpotential curve was obtained around −0.31 V *vs.* RHE, as shown in the inset of Fig. 10. These findings reflect, besides its superior HER catalytic activity, the high stability and durability of our best catalyst (alloy II pre-treated by pitting corrosion).

4. Conclusion

The effect of alloyed Al addition (1.0 wt%) on the corrosion and electrochemical behavior of CoNiGa magnetic shape memory alloy was studied in 0.5 M NaCl solutions, employing various electrochemical techniques. Alloyed Al was found to enhance uniform corrosion of the tested MSMA. In this respect, Tafel extrapolation and linear polarization resistance methods showed an obvious increase in the uniform corrosion rate in presence of alloyed Al. Impedance measurements performed at the corrosion potential (E_{corr}) came to the same conclusion and showed that the addition of Al to the tested MSMA decreased the total impedance (Z). Alloyed Al has also weakened passivity, and hence accelerated pitting attack induced by aggressive Cl^- anions, of the studied MSMA, as evidenced from cyclic polarization and chronoamperometry measurements. XPS studies confirmed weakness of passivity in presence of Al, which was translated to enhanced adsorption of Cl^-. Uniform and pitting corrosion processes promoted by alloyed Al were also supported from morphological studies based on SEM. Alloyed Al also increased the cathodic hydrogen evolution kinetics on the tested MSMA, as revealed by cathodic polarization and impedance measurements in 0.1 M KOH solutions. The electrocatalytic activity of CoNiGaAl MSMA towards the hydrogen evolution reaction in the KOH solutions was further improved approaching that of Pt/C *via* 24 h of free corrosion pre-treatment in 0.5 M NaCl solution at room temperature. Such corrosion pre-treatment has resulted in intense pitting attack. These results reveal that the combination of surface roughness (due to pitting corrosion catalyzed by alloyed Al) and high crystallinity (due to the martensite phase formation induced by alloyed Al) are highly beneficial for the greatly enhanced electrocatalytic activity of the pitted CoNiGaAl MSMA, which also exhibited good stability and durability.

References

1 H. E. Karaca, I. Karaman, Y. I. Chumlyakov, D. C. Lagoudas and X. Zhang, *Scr. Mater.*, 2004, **51**, 261–266.
2 H. E. Karaca, I. Karaman, D. C. Lagoudas, H. J. Maier and Y. I. Chumlyakov, *Scr. Mater.*, 2003, **49**, 831–836.
3 D. Meyer, H. J. Maier, J. Dadda, I. Karaman and H. E. Karaca, *Mater. Sci. Eng., A*, 2006, **438–440**, 875–878.
4 V. A. Chernenko, E. Cesari, V. V. Kokorin and I. N. Vitenko, *Scr. Mater.*, 1995, **33**, 1239–1244.
5 K. Ullako, J. K. Huang, C. Kantner, R. C. O'Handley and V. V. Kokorin, *Appl. Phys. Lett.*, 1996, **69**, 1966–1968.
6 S. J. Murray, M. Marioni, S. M. Allen and R. C. O'Handley, *Appl. Phys. Lett.*, 2000, **77**, 886–888.
7 A. Sozinov, A. A. Likhachev, N. Lanska and K. Ullakko, *Appl. Phys. Lett.*, 2002, **80**, 1746–1748.
8 E. Bonnot, R. Romero, L. Mañosa, E. Vives and A. Planes, *Phys. Rev. Lett.*, 2008, **100**, 125901.
9 A. Planes, L. Manosa and M. Acet, *J. Phys.: Condens. Matter*, 2009, **21**, 233201.
10 K. A. Gschneidner Jr, V. Pecharsky and A. Tsokol, *Rep. Prog. Phys.*, 2005, **68**, 1479.
11 R. D. James and M. Wuttig, *Philos. Mag. A*, 1998, **77**, 1273–1299.
12 T. Kakeshita, T. Takeuchi, T. Fukuda, T. Saburi, R. Oshima, S. Muto and K. Kishio, *Mater. Trans., JIM*, 2000, **41**, 882–887.
13 F. Gejima, Y. Sutou, R. Kainuma and K. Ishida, *Metall. Mater. Trans. A*, 1999, **30**, 2721–2723.
14 K. Oikawa, L. Wulff, T. Iijima, F. Gejima, T. Ohmori, A. Fujita, K. Fukamichi, R. Kainuma and K. Ishida, *Appl. Phys. Lett.*, 2001, **79**, 3290–3292.
15 H. Morito, A. Fujita, K. Fukamichi, R. Kainuma, K. Ishida and K. Oikawa, *Appl. Phys. Lett.*, 2002, **81**, 1657–1659.
16 S. Kaul, B. A. D'Santhoshini, A. Abhyankar, L. F. Barquin and P. Henry, *Appl. Phys. Lett.*, 2006, **89**, 093119.
17 K. Oikawa, T. Ota, F. Gejima, T. Ohmori, R. Kainuma and K. Ishida, *Mater. Trans., JIM*, 2001, **42**, 2472–2475.
18 A. Gebert, S. Roth, S. Oswald and L. Schultz, *Corros. Sci.*, 2009, **51**, 1163–1171.
19 M. A. Amin, N. El-Bagoury and H. Shokry, *Int. J. Electrochem. Sci.*, 2013, **8**, 2791–2805.
20 L. L. Stepan, D. S. Levi, E. Gans, K. P. Mohanchandra, M. Ujihara and G. P. Carman, *J. Biomed. Mater. Res., Part A*, 2007, **82**, 768–776.
21 P. Paunovic, O. Popovski, S. Hadzi Jordanov, A. Dimitrov and D. Slavkov, *J. Serb. Chem. Soc.*, 2006, **71**, 149–165.
22 P. Elumalai, H. N. Vasan, N. Munichandraiah and S. A. Shivashankar, *J. Appl. Electrochem.*, 2002, **32**, 1005–1010.
23 L. D. Rafailovic, C. Gammer, C. Rentenberger, C. Kleber, A. H. Whitehead, B. Gollas and H. P. Karnthaler, *Phys. Chem. Chem. Phys.*, 2012, **14**, 972–980.
24 J. Deng, P. Ren, D. Deng and X. Bao, *Angew. Chem., Int. Ed.*, 2015, **54**, 2100–2104.
25 M. Sanchez-Carrillo, J. P. Flores de los Rios, E. Huape-Padilla, R. G. Bautista Margulis, H. Flores-Zuniga, M. I. Ferrer-Sanchez, G. Lopez-Ocana, L. G. Chacon-Nava and A. Martinez-Villafane, *Int. J. Electrochem. Sci.*, 2014, **9**, 7725–7735.
26 ASTM G 31, *Standard Practice for Laboratory Immersion Corrosion Testing of Metals*, Licensed for BASF, p. 5.
27 J. A. Richardson and G. C. Wood, *Corros. Sci.*, 1970, **10**, 313–323.
28 A. Kolics, J. C. Polkinghorne and A. Wieckowski, *Electrochim. Acta*, 1998, **43**, 2605–2618.
29 Z. A. Foroulis and M. J. Thubrikar, *J. Electrochem. Soc.*, 1975, **122**, 1296–1301.
30 R. T. Foley and T. H. Nguyen, *J. Electrochem. Soc.*, 1982, **129**, 464–467.

 This journal is © The Royal Society of Chemistry 2017

Open Access Article. Published on 13 January 2017. Downloaded on 10/20/2025 1:41:01 AM.
This article is licensed under a Creative Commons Attribution 3.0 Unported Licence.

31 T. P. Hoar, *Corros. Sci.*, 1967, **7**, 341–355.
32 Z. Szklarska-Smialowska, *Pitting Corrosion of Metals*, NACE, Houston, TX, 1986.
33 M. A. Amin, H. H. Hassan and S. S. Abd El Rehim, *Electrochim. Acta*, 2008, **53**, 2600–2609.
34 M. A. Amin, S. S. Abd El Rehim and A. S. El-Lithy, *Corros. Sci.*, 2010, **52**, 3099–3108.
35 A. G. Munoz and J. B. Bessone, *Corros. Sci.*, 1999, **41**, 1447–1463.
36 V. Moutarlier, M. P. Gigandet and J. Pagetti, *Appl. Surf. Sci.*, 2003, **206**, 237–249.
37 Z. Szklarska-Smialowska, *Corros. Sci.*, 1999, **41**, 1743–1767.
38 M. A. Amin, *Electrochim. Acta*, 2011, **56**, 2518–2531.
39 M. A. Amin, N. El-Bagoury, M. Saracoglu and M. Ramadan, *Int. J. Electrochem. Sci.*, 2014, **9**, 5352–5374.
40 M. A. Amin, S. S. Abd El-Rehim, E. E. F. El-Sherbini, S. R. Mahmoud and M. N. Abbas, *Electrochim. Acta*, 2009, **54**, 4288–4296.
41 N. El-Bagoury, M. A. Amin and M. Saracoglu, *Int. J. Electrochem. Sci.*, 2015, **10**, 5291–5308.
42 A. J. Bard and L. R. Faulkner, *Electrochemical Methods: Fundamental and Applications*, John Wiley and Sons, Inc, New York, 2001.
43 C. Lupi, A. Dell'Era and M. Pasquali, *Int. J. Hydrogen Energy*, 2009, **34**, 2101–2106.
44 F. Safizadeh, E. Ghali and G. Houlachi, *Int. J. Hydrogen Energy*, 2015, **40**, 256–274.
45 F. Rosalbino, S. Delsante, G. Borzone and E. Angelini, *Int. J. Hydrogen Energy*, 2008, **33**, 6696–6703.
46 M. M. Jaksic, *Int. J. Hydrogen Energy*, 2001, **26**, 559–578.
47 M. Xia, T. Lei, N. Lv and N. Li, *Int. J. Hydrogen Energy*, 2014, **39**, 4794–4802.
48 R. Solmaz and G. Kardas, *Int. J. Hydrogen Energy*, 2011, **34**, 12079–12087.
49 L. M. Rodrıguez-Valdez, I. Estrada-Guel, F. Almeraya-Calderon, M. A. Neri-Flores, A. Martınez-Villafane and R. Martınez-Sanchez, *Int. J. Hydrogen Energy*, 2004, **29**, 1141–1145.
50 A. Barbucci, G. Cerisola and P. L. Cabot, *J. Electrochem. Soc.*, 2002, **149**, B534–B542.
51 Q. Lu, G. Hutchings, W. Yu, Y. Zhou, R. Forest, R. Tao, J. Rosen, B. Yonemoto, Z. Cao, H. Zheng, J. Xiao, F. Jiao and J. Chen, *Nat. Commun.*, 2015, **6**, 6567–6574.
52 J. Durst, A. Siebel, C. Simon, F. Hasché, J. Herranz and H. A. Gasteiger, *Energy Environ. Sci.*, 2014, **7**, 2255–2260.
53 E. A. Franceschini, G. I. Lacconi and H. R. Corti, *Electrochim. Acta*, 2015, **159**, 210–218.
54 D. Delgado, G. Hefter and M. Minakshi, Hydrogen Generation, in *Alternative Energies*, ed. G. Ferreira, Springer, Berlin, 2013, pp. 141–161.
55 P. Elumalai, H. N. Vasan, N. Munichandraiah and S. A. Shivashankar, *J. Appl. Electrochem.*, 2002, **32**, 1005–1010.
56 G. Darabdhara, M. A. Amin, G. A. M. Mersal, E. M. Ahmed, M. R. Das, M. B. Zakaria, V. Malgras, S. M. Alshehri, Y. Yamauchi, S. Szunerits and R. Boukherroub, *J. Mater. Chem. A*, 2015, **3**, 20254–20266.
57 M. A. Amin, S. A. Fadlallah and G. S. Alosaimi, *Int. J. Hydrogen Energy*, 2014, **39**, 19519–19540.
58 M. A. Amin, S. A. Fadlallah, G. S. Alosaimi, F. Kandemirli, M. Saracoglu, S. Szunerits and R. Boukherroub, *Int. J. Hydrogen Energy*, 2016, **41**, 6326–6341.
59 B. Losiewicz, A. Budniok, E. Rowinski, E. Lagiewka and A. Lasia, *Int. J. Hydrogen Energy*, 2004, **29**, 145–157.
60 C. González-Buch, I. Herraiz-Cardona, E. M. Ortega, J. García-Antón and V. Pérez-Herranz, *Chemical Engineering Transactions*, 2013, **32**, 865–870.
61 X. Wu, H. Ma, S. Chen, Z. Xu and A. Sui, *J. Electrochem. Soc.*, 1999, **146**, 1847–1853.
62 H. Ma, S. Chen, B. Yin, S. Zhao and X. Liu, *Corros. Sci.*, 2003, **45**, 867–882.
63 Z. B. Stoynov, B. M. Grafov, B. Savova-Stoynova and V. V. Elkin, *Electrochemical Impedance*, Nanka, Moscow, 1991.
64 F. B. Growcock and R. J. Jasinski, *J. Electrochem. Soc.*, 1989, **136**, 2310–2314.
65 M. Monev, *Bulg. Chem. Commun.*, 2016, **48**, 73–77.
66 D. M. Soares, O. Teschke and I. Torriani, *J. Electrochem. Soc.*, 1992, **139**, 98–105.
67 D. S. Hall, C. Bock and B. R. MacDougalla, *J. Electrochem. Soc.*, 2013, **160**, F235–F243.
68 C. Lupi, A. Dell'Era and M. Pasquali, *Int. J. Hydrogen Energy*, 2014, **39**, 1932–1940.
69 F. Rosalbino, D. Macciò, A. Saccone and G. Scavino, *Int. J. Hydrogen Energy*, 2014, **39**, 12448–12456.
70 W. Ben Aziza, J. F. Petit, U. B. Demirci, Q. Xu and P. Miele, *Int. J. Hydrogen Energy*, 2014, **39**, 16919–16926.
71 M. I. Jamesh, *J. Power Sources*, 2016, **333**, 213–236.
72 S. H. Hong, S. H. Ahn, I. Choi, S. G. Pyo, H.-J. Kim, J. H. Jang and S.-K. Kim, *Appl. Surf. Sci.*, 2014, **307**, 146–152.
73 V. Bachvarov, E. Lefterova and R. Rashkov, *Int. J. Hydrogen Energy*, 2016, **41**, 12762–12771.
74 H. S. Shatak, *Corrosion of Austenitic Stainless Steel*, Narosa Publishing House, London, 2002, p. 41.
75 B. M. Gonzalez, C. S. B. Castro, V. T. L. Buono, J. M. C. Vilela, M. S. Andrade, J. M. D. Moraes and M. J. Mantel, *Mater. Sci. Eng., A*, 2003, **343**, 51–56.
76 F. S. Shieu, M. J. Deng and S. H. Lin, *Corros. Sci.*, 1998, **40**, 1267–1279.
77 M. C. Biesinger, B. P. Paynec, A. P. Grosvenor, L. W. M. Laua, A. R. Gerson and R. S. C. Smart, *Appl. Surf. Sci.*, 2011, **257**, 2717–2730.
78 D. Briggs, XPS: Basic Principles, Spectral Features and Qualitative Analysis, in *Surface Analysis by Auger and X-ray Photoelectron Spectroscopy*, ed. D. Briggs and J. T. Grant, IM Publications, Chichester, 2003, pp. 31–56.
79 J. F. Xie, H. Zhang, S. Li, R. X. Wang, X. Sun, M. Zhou, J. F. Zhou, X. W. Lou and Y. Xie, *Adv. Mater.*, 2013, **25**, 5807–5813.